III–V/Silicon Hybrid Non-linear Nanophotonics in the Context of On-Chip Optical Signal Processing and Analog Computing

Léa Constans[1,2]*, Sylvain Combrié[1], Xavier Checoury[2], Grégoire Beaudoin[2], Isabelle Sagnes[2], Fabrice Raineri[2,3] and Alfredo de Rossi[1]

[1] Thales Research and Technology, Palaiseau, France, [2] Centre de Nanosciences et de Nanotechnologies (C2N), CNRS, Univ Paris Sud, Université Paris-Saclay, Palaiseau, France, [3] Université de Paris, Centre de Nanosciences et de Nanotechnologies, Palaiseau, France

We discuss the application of silicon hybrid photonic integration technology for all-optical signal processing. The core is a photonic crystal nanocavity made of a III–V semiconductor alloy. This ensures ultra-fast and energy-efficient all-optical operation, which is crucial for scaling from a single device to a non-linear photonic processor where ideally a large number of non-linear elements cooperate. We discuss all-optical sampling as an immediate application of this technology and give an example of a future non-linear integrated circuit based on this technology.

1. INTRODUCTION

Over the last decade, the increasing demand in bandwidth for communication and data processing has stimulated the emergence of alternative computing paradigms [1]. In this context, it has been suggested that photonic technologies such as optical interconnects [2] will address the large scale challenge in high performance computing [3]. Even more recently, research is focusing on neuro-inspired photonic circuits, for instance to implement deep convolutional networks [4] or reservoir computing [5]. Electro-optic photonic circuits with an electronic feedback or control have been considered here because the technology is available and already well-mastered. Reservoir computing or convolutional neural networks are however inherently non-linear systems [6] and a truly all-optical implementation would require a non-linear optical element. Moreover, all-optical signal processing removes the need of two-way conversion between the optical and the electronic domain whenever the information carried by the optical signal needs to be analyzed. Consider for instance a network where optical signals are exchanged between a multitude of nodes, according to the address carried at the head of a message, which has long been investigated in optical communication [7]. Avoiding unnecessary conversion on one hand, and integration on the other are of paramount importance to improve energy efficiency in communications and computing; therefore, the integration of energy efficient all-optical signal processing in a photonic chip is highly desirable in this context.

Here we discuss a novel integrated technology implementing an all-optical gate (AOG), a general purpose device acting on an incoming optical signal under the control of another optical signal, which necessarily relies upon a non-linear optical effect. There is a broad range of effects resulting into a non-linear optical response, with a general rule trading a fast response with a large power

density. Energy-efficient AOGs are therefore challenging. Exploiting the long interaction length possible in non-linear fibers has enabled ultra fast AOGs, known as non-linear fiber loops [8]. A more compact implementation is based on the non-linear response of semiconductor optical amplifiers (SOAs), using four wave mixing (FWM), cross gain or cross phase modulation (XGM and XPM) [9, 10]. The non-linear response can also arise from the dependence of the refractive index on the population of free carriers. In contrast to the electronic Kerr effect, this is slower but much stronger and it is therefore preferred for switching. A potentially more compact solution is based on passive semiconductor photonic circuits, whereby resonant enhancement compensates for a weaker non-linear response [11]. With the emergence of silicon photonics it has been pointed out how desirable is the availability of all-optical switching on this platform [12].

The assumption that the properties of silicon and the geometries of the resonators commonly available in silicon photonics are the most suitable for an ultra-fast and energy-efficient AOG is however questionable. First, the resonant enhancement of the electromagnetic field in resonators scales as QV^{-1} with Q the quality factor of the resonator and V the modal volume. So the more confined the optical mode in the gate and the larger the Q-factor, the lower the switching energy, which is a strong reason for considering photonic crystal (PhC) cavities [13], as they feature strongly confined optical modes, down to the diffraction limit $(\lambda/n)^3$ [14], as well as ultrahigh Q-factors up to $11 \cdot 10^6$ [15].

PhC are patterned dielectrics with sub-wavelength features resulting into a large surface to volume ratio. This greatly enhances the role of surfaces, in particular in accelerating the dynamics of free carriers, which results into a much faster non-linear response. All-optical modulation in an AOG, where optical inputs are in the Telecom wavelength range and travel in plane, has been demonstrated in a silicon PhC cavity with switching time in the range of 100 ps [16]. Free carriers in PhCs made of GaAs have been found to relax much faster [17]. Thus, the combination of a faster non-linearity with an optimized cavity led to an all-telecom all-optical device with < 10 ps response and very low energy per bit (100 fJ) [18]. The variety of semiconductor alloys of the III–V group allows further optimization, hence allowing a record low energy-per-bit consumption with a quaternary InGaAsP alloy [19], which eloquently demonstrates the benefit of III–V materials for all-optical signal processing. This makes a very strong case for the integration of III–V based AOGs in a silicon Photonic circuit, a mandatory requirement for addressing the complexity of photonic integration. This squarely falls within the domain of the hybrid photonic technologies, which have been developed for the integration of optical sources, necessarily based on III-V alloys. A very successful and versatile technology is based on wafer bonding techniques [20] which have been also capable of integrating photonic nanostructures. This paved the way to ultra-low power and compact nanolaser diodes on a silicon photonic platform [21]. Based on the heterogeneous integration of III–V photonic nanostructures, fast and efficient AOGs have

been demonstrated [22], which opens the perspective of high-density and energy-efficient photonic circuits for all-optical signal processing.

This article describes the operation of AOGs based on a III–V on silicon (III–V/Si) hybrid nanophotonics as well as the underlying physical phenomena, and considers the perspective of integrated all-optical signal processing circuits. It is organized as follows: first we present in section 1 the working principle of an AOG based on an optical resonator. In section 2 we describe our hybrid III–V/Si PhC-based AOG and show its non-linear properties, and finally examples of application of these AOGs are given in section 3 and in the conclusion, respectively all-optical sampling and integrated non-linear all-optical processing.

2. ALL-OPTICAL GATE BASED ON A SEMICONDUCTOR RESONATOR

An AOG based on an optical resonator or cavity works as illustrated in **Figure 1**. The system is composed of a resonator and a waveguide. The waveguide carries the optical signal (λ_s) to be processed as well as the optical control signal (λ_c), and the light is coupled to the resonator by evanescent waves, meaning a coupling distance, or distance between the waveguide and the resonator shorter than the wavelength of the signals. The resonator can be in-line or side-coupled to the waveguide, and without loss of generality, we consider here the side-coupled configuration. The system is designed so that the wavelength of the signal λ_s is tuned to a resonant mode of the cavity. Consequently, in the side-coupled configuration, the transmission of the signal through the gate is weak, corresponding to an OFF-state. The role of the control signal is to open the gate: each pulse sent to the gate induces a non-linear effect in the cavity which results in a spectral shift of all the resonances. The signal is then off-resonance, and its transmission through the gate increases, leading to an ON-state.

The usual non-linear effects used in photonic structures are either Kerr effects or free-carrier effects. Although Kerr effects are much faster, free-carrier effects can be much stronger as we show below, and consequently much energy-efficient. Among free-carrier effects, the non-linear index change following the concentration of free carriers, or free carrier dispersion (FCD) is a well-known effect in the context of photonic devices (electro-optic modulators and switches) and it has been very accurately modeled for some materials, in particular InP, GaAs and InGaAsP at telecom wavelengths [23]. The strength of the effect, or the magnitude of $\frac{\partial n}{\partial N}|_{FCD}$, with n the refractive index and N the number of free carriers, depends on the proximity to the edge of the electronic bandgap. For instance in InP, for photon energies close to the bandgap, another free-carrier effect, namely band-filling, dominates, whereas for much smaller energies the more general FCD described by the Drude model contributes [23]. In both cases, the refractive index decreases with increasing free carrier population, which induces a blue shift of the optical resonances. When considering the limit of long pulses compared to the carrier lifetime τ_c, one can obtain a "Kerr-equivalent"
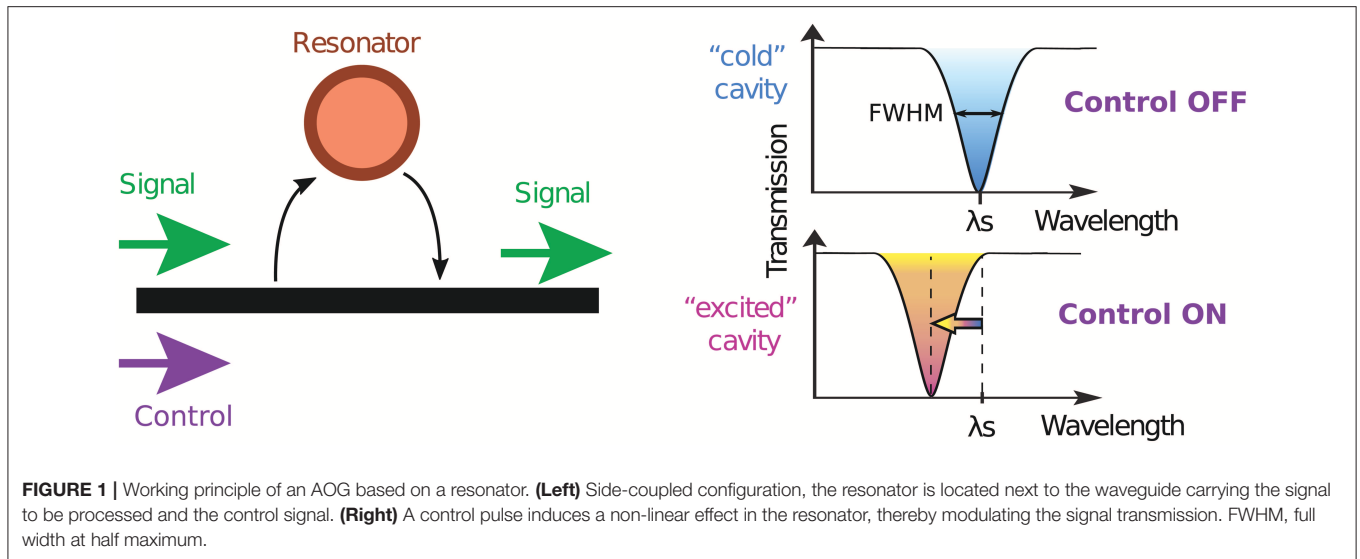
FIGURE 1 | Working principle of an AOG based on a resonator. **(Left)** Side-coupled configuration, the resonator is located next to the waveguide carrying the signal to be processed and the control signal. **(Right)** A control pulse induces a non-linear effect in the resonator, thereby modulating the signal transmission. FWHM, full width at half maximum.

non-linearity of a few orders of magnitude stronger than actual Kerr effects. One can write:

$$n_{2,FC} = n_{FC} \frac{\alpha \tau_c}{\hbar \omega} \qquad (1)$$

with $n_{2,FC}$ the "Kerr-equivalent" non-linearity, n_{FC} the free-carrier non-linearity, α the absorption term (here linear), and $\hbar \omega$ the photon energy. As an example, in InGaAsP, assuming $n_{FC} = \frac{\partial n}{\partial N}|_{FCD} = -8.10^{-26} \, \text{m}^3$, $\alpha \approx 300 \, \text{m}^{-1}$, $\tau_c \approx 100$ ps and incident light at 1550 nm, one obtains $n_{2,FC} \approx 2.10^{-14} \, \text{m}^2 W^{-1}$, compared to Kerr non-linearity $n_2 = 3.10^{-16} \, \text{m}^2 W^{-1}$ [24]. From now on, the non-linear effect employed in all-optical gates mentioned in this article will be FCD, unless precised otherwise.

In an AOG, free carriers are injected upon absorption of the control signal. In order to obtain a high transmission contrast of the gate, the spectral shift of the cavity resonance should be comparable to its linewidth (or FWHM, full width at half maximum), as illustrated in **Figure 1**. To do so, a sufficiently large energy has to be injected and absorbed in the cavity to reach the required density of free carriers. If a total energy U is sent to the cavity, then the density of electromagnetic energy W in the cavity writes $W = \frac{U}{V_{mod}}$, with V_{mod} the modal volume of the cavity modes. Knowing that the modal volume decreases from about $10^{-8} \, \text{cm}^3$, typical of Fabry-Perot laser diodes, to $4 \cdot 10^{-14} \, \text{cm}^3$ for a PhC cavity [14], the required energy will be more than five orders of magnitude smaller in the latter. Specifically, the target carrier density is about $10^{17} \, \text{cm}^{-3}$, which would require the absorption of about $4 \cdot 10^3$ telecom photons, which corresponds to about 1 fJ.
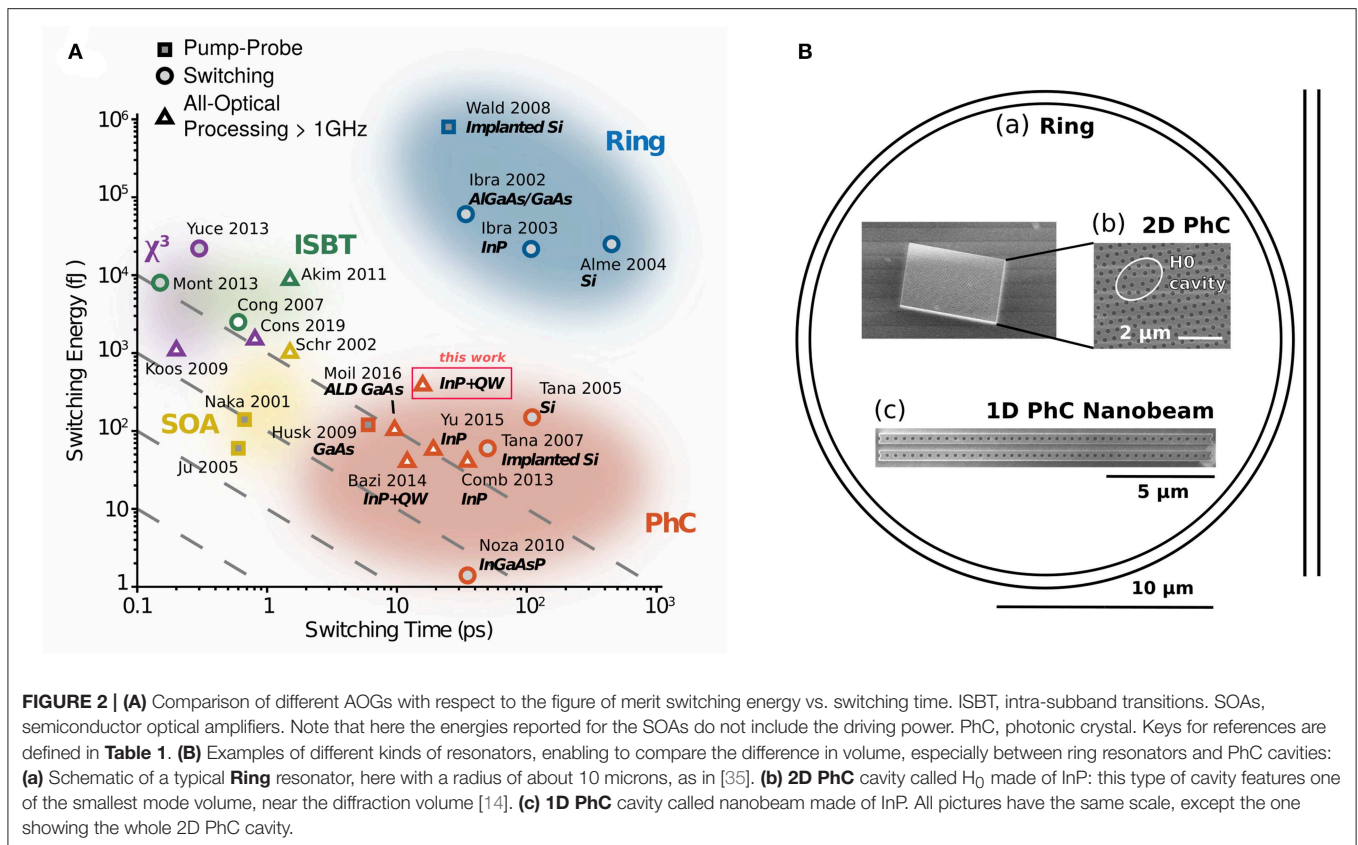
A more accurate estimate considers the spectral shift required to change the transmission from a minimum to a maximum, which equals $\approx$ FWMH $= \frac{\nu}{Q}$, and leading to the corresponding carrier density N. Combining with the mode volume this gives:

$$U = \frac{h\nu^2 V_{mod}}{Q \frac{\partial \nu}{\partial N}|_{FCD}} = \frac{h\nu V_{mod}}{2\pi \tau \frac{\partial \nu}{\partial N}|_{FCD}} \qquad (2)$$

where ν is the frequency of photons, h the Plank's constant, Q the quality factor of the cavity and τ the photon lifetime according to $2\pi \tau \nu = Q$. Note that the photon lifetime sets the lower limit to the time response of the AOG. This equation evidences that the product $U \cdot \tau$ is basically constant once the geometry (V_{mod}) and the material ($\frac{\partial \nu}{\partial N}$) are fixed. Thus, the best way to reduce the switching energy with no loss of speed is to reduce the modal volume of the resonator. This is illustrated in **Figure 2** which plots the performance of different types of AOGs, following the figure of merit switching energy vs. speed. By passing from ring resonators to more compact PhC cavities, like 1D PhC "nanobeams" [42] or even more confined H_0 cavity [18], the switching energy has been reduced from about 10^4 fJ to a several tens of fJ, and even sub-fJ energies using an optimized quaternary alloy [19]. Moreover, there was no degradation of the speed, featuring about 50 ps switching time in average and even shorter than 10 ps for GaAs-based PhC cavities [18, 41]. It is apparent from the figure that PhC-based AOGs use much less energy than ring resonators in general, which is clearly related to a much smaller mode volume. They are also faster, because carrier dynamics is accelerated by the strong surface recombination. The connection to the surface/volume ratio is apparent: in typical PhC slabs, the typical distance L to the closest surface is 100 nm, when the diffusion length in bulk semiconductor is about 1 μm. Bulk recombination becomes thus negligible compared to surface recombination, which is well-captured by the Schockley model [43]:

$$\tau_{carriers}^{-1} = \tau_{bulk}^{-1} + SL^{-1} \approx SL^{-1} \qquad (3)$$

with $\tau_{carriers}$ the carrier lifetime in the PhC, τ_{bulk} the carrier lifetime in bulk semiconductor, and S the surface recombination velocity. The carrier relaxation time, hence the switching speed, depend critically on S, which has been confirmed through more accurate calculations in Tanabe et al. [44]. Surface recombination velocity can be modified, hence optimized through surface passivation (slowing down dynamics) or by adding a layer with

FIGURE 2 | (A) Comparison of different AOGs with respect to the figure of merit switching energy vs. switching time. ISBT, intra-subband transitions. SOAs, semiconductor optical amplifiers. Note that here the energies reported for the SOAs do not include the driving power. PhC, photonic crystal. Keys for references are defined in **Table 1**. **(B)** Examples of different kinds of resonators, enabling to compare the difference in volume, especially between ring resonators and PhC cavities: **(a)** Schematic of a typical **Ring** resonator, here with a radius of about 10 microns, as in [35]. **(b) 2D PhC** cavity called H_0 made of InP: this type of cavity features one of the smallest mode volume, near the diffraction volume [14]. **(c) 1D PhC** cavity called nanobeam made of InP. All pictures have the same scale, except the one showing the whole 2D PhC cavity.

stronger recombination velocity. The latter has been used to reduce the relaxation time in InP based PhC down to about 15 ps [22]. Conversely, surface passivation by atomic-layer deposition (ALD) was employed to increase the very fast carrier lifetime of GaAs from 1 to 10 ps, allowing larger non-linear effect in the cavity [41]. Indeed, if a long carrier lifetime limits the operation frequency of the gate, a too short lifetime in contrast prevents from inducing a large non-linear effect due to a too weak carrier photogeneration, limiting the dynamical contrast of the AOG. Besides surface recombination, p-doping a III–V semiconductor to allow only the much faster electrons to move also results in a substantial acceleration of the dynamics. This has been also demonstrated with PhC cavities [45] decreasing the switching time to 30 ps. Note that the time decay of the non-linear process can be shorter than the carrier lifetime, owing to the fact that two different processes lie behind carriers dynamics: diffusion and recombination. In very compact PhC cavities which display highly confined optical modes, the initial small volume where carriers are generated results in a high carrier density gradient, leading to a very fast diffusion in the material. In this case the decay of the non-linear effect is dominated by this fast diffusion, and thus characterized by decay time that can be several times shorter than the real carrier lifetime in the structure, like switching times of 20–50 ps in an InGaAsP 2D PhC cavity compared to initial carrier lifetime of hundreds of picoseconds [19]. A different yet effective strategy to increase the speed of AOGs is to introduce a Fano-like resonance, resulting in a strongly asymmetric lineshape. This also results into a larger

transmission contrast when keeping energy and material fixed and has been demonstrated to be very effective for all-optical switching [40, 46].

To sum up, in order to optimize the performance of compact AOGs based on optical resonators, the volume must be reduced to decrease the needed switching energy, which can be done by playing with the geometry of the resonator, or with the switching transfer function using for instance Fano resonances. The choice of the material enables also to tune the non-linearity efficiency, as well as the dynamics of the gate. When looking at **Figure 2**, it can clearly be seen that PhC-based AOGs are very close to reach the same performance of much bigger and energy consuming devices such as SOAs [27] and thus address the challenges of fast all-optical signal processing and computing in an integrated platform.

3. LINEAR AND NON-LINEAR PROPERTIES OF HYBRID III–V/SI ALL-OPTICAL GATES BASED ON PHC CAVITY

The development and mastery of various wafer bonding techniques and in particular III-V/Si nanostructures [20, 47] make III–V materials relevant candidates to build optical devices that can be integrated on a silicon photonic platform, such as nanolaser diodes [21], Mach-Zehnder modulators [48], memories for flip-flop operation [49], or all-optical switches [22]. We will hereafter consider the technology developed in

TABLE 1 | AOG technologies.

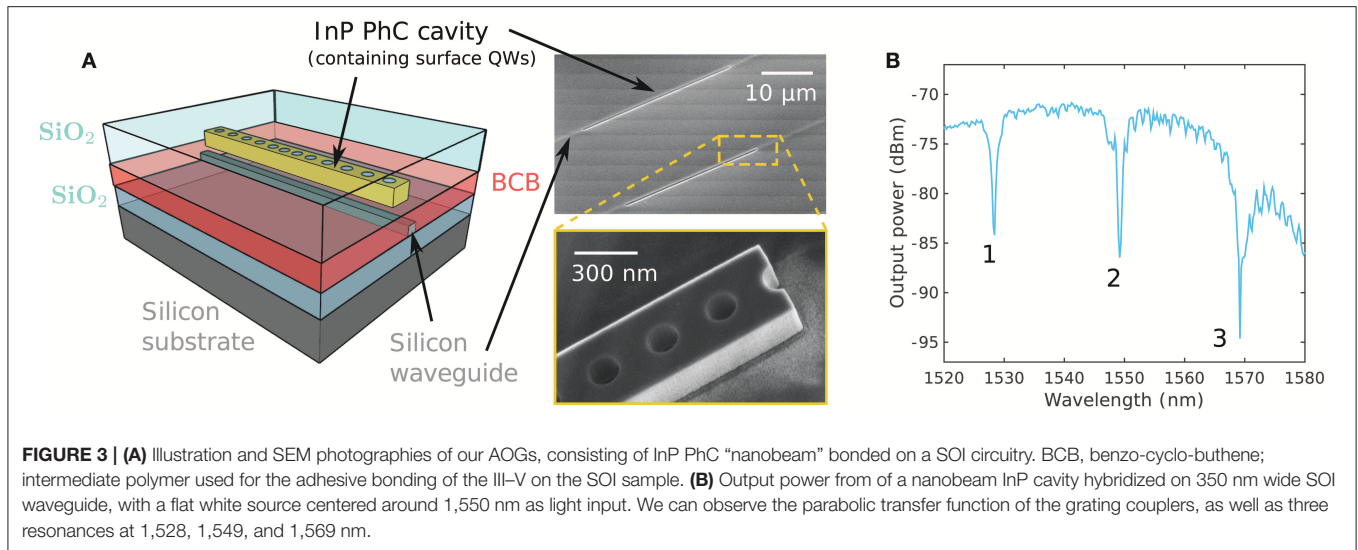| Key	Description	References
SOA		
Naka2001	InGaAsP, intraband effects	[25]
Schr2002	InGaAsP, XGM-XPM	[26]
Ju2005	InGaAsP/InGaAs, non-lin. polar. rotation	[27]
χ³		
Koos2009	Hybrid silicon-organic	[28]
Yuce2013	GaAs-AlAs microcavity	[29]
Cons2019	Hybrid InGaP on silicon	[30]
ISBT		
Cong2007	(CdS/ZnSe)/BeTe	[31]
Akim2011	InGaAs/AlAsSb QWs	[32]
Mont2013	GaN/AlN QDs	[33]
RING RESONATOR		
Ibra2002	AlGaAs ring resonator	[34]
Ibra2003	InP ring resonator	[35]
Alme2004	Silicon ring resonator	[36]
Wald2008	Implanted silicon	[37]
PHOTONIC CRYSTAL		
Tana2005	Silicon	[16]
Tana2007	Implanted silicon	[38]
Husk2009	GaAs	[18]
Noza2010	InGaAsP	[19]
Comb2013	InP	[39]
Bazi2014	InP + QW on silicon	[22]
Yu2015	InP Fano PhC	[40]
Moil2016	GaAs PhC + ALD	[41]

the latter reference. The III–V nanoresonator is heterogeneously integrated on a silicon-on-insulator (SOI) circuitry using adhesive bonding through a thin layer of polymer (benzo-cyclo-buthene or BCB), following the same process as in Bazin et al. [22]. The structure is shown in **Figure 3A**: it is made of a few (typically 10) micrometer long rib with sub-wavelength (650 × 260 nm) cross section and an apodized periodic pattern of holes, which are patterned above the SOI waveguides by electronic writing and inductively-coupled plasma (ICP) etching. The structure is then entirely encapsulated with SiO_2. Thin surface layers of InGaAs drastically enhance surface recombination, by more than one order of magnitude than in bare InP [50], resulting into a short carrier lifetime which varies between 10 and 30 ps [22].

A crucial aspect of the design is the apodization of the periodic pattern, which is optimized to minimize radiative leakage [42], a critical aspect in periodic structures embedded in a solid cladding. The design consists in a row of holes with constant radius (120 nm) and increasing period from a minimum which is here around 350 nm, but which can be adjusted to precisely target a resonance frequency. The apodization creates an effective "potential well" for photons which is adjusted to define the spatial width of the cavity mode. This also determines the free spectral ranges between resonances, which is here tuned to obtain two resonances around 1,550 nm, separated by about 10 to 20 nm.

The cavity is evanescently coupled to the underlying silicon rib waveguide shown in **Figure 3A**, with a coupling distance of 350 nm. The coupling strength is controlled by the accurate vertical alignment (better than a few tens of nm) of the cavity and the waveguide; the coupling strength can be increased relatively to the intrinsic loss ($Q_{int} \approx 10^5$ typically [51]) in order to set the resonator in the strongly overcoupled configuration, thereby ensuring very low coupling losses.

For the purpose of optical characterization, the sample is accessed from optical fibers to the gate via grating couplers at the SOI waveguide edges, and the angle of the fibers is optimized to set the maximum of the couplers transmission at a wavelength near the first order modes of the cavity. Each grating coupler brings 7 to 8 dB losses at their transmission maximum, which accounts almost totally for the transmission losses of the gates, because the propagation losses of the SOI waveguides reach 2.4 dB/cm and the waveguides are <1-cm long. An example of raw transmission spectrum shown in **Figure 3B**, which here has not been corrected with the parabolic response of the grating couplers, reveals three resonances, corresponding to transmission minima at 1,528, 1,549, and 1,569 nm, with loaded quality factors equal to 860, 620, and 100, respectively. So the losses of the loaded cavity are much higher than the intrinsic losses to ensure strong overcoupling as mentioned above, hence a large transmission contrast (resonances' minima are at least 10 dB below transmission). This also enables to set the photon lifetime τ in the cavity to be about 1 ps, a fraction of the effective carrier lifetime, in order to avoid further increase of the switching time. As discussed in the previous section with Equation (2), with this choice we trade speed (τ) for energy efficiency (U), as here the cavity lifetime is about one order of magnitude shorter than in the all-optical switching experiment [22]. From the transmission contrast (minimum transmission T_0 at resonance, normalized such that $T = 1$ out of resonance), intrinsic Q factors are extracted through $Q_{int} = \frac{Q}{\sqrt{T_0}}$, namely 3,200, 2,500, and 500. Unlike suspended PhC cavities which can feature very high Q-factors of several millions [15], not suspended membranes show lower Q-factors, up to more than a couple million in silicon [52]. Looking at the same type of cavity as the ones we use, an intrinsic Q-factor of 10^5 was obtained in a not suspended PhC cavity made of InP [51]. In comparison, intrinsic losses in our cavities are much larger, and we believe that the losses are dominated by linear absorption induced by the InGaAs layers. Consequently the scattering losses alone should be as low as in similar structures with InGaAs layers like in Bazin et al. [22], where they obtained an intrinsic Q-factor of 17,000. But it should be pointed out that very high Q-factors are not needed for switching functions, because this would limit the speed operation of the gate due to long photon lifetime in the cavity. Here intrinsic Q-factors of the order of 10^4 are sufficient to ensure both low losses and a short time response.
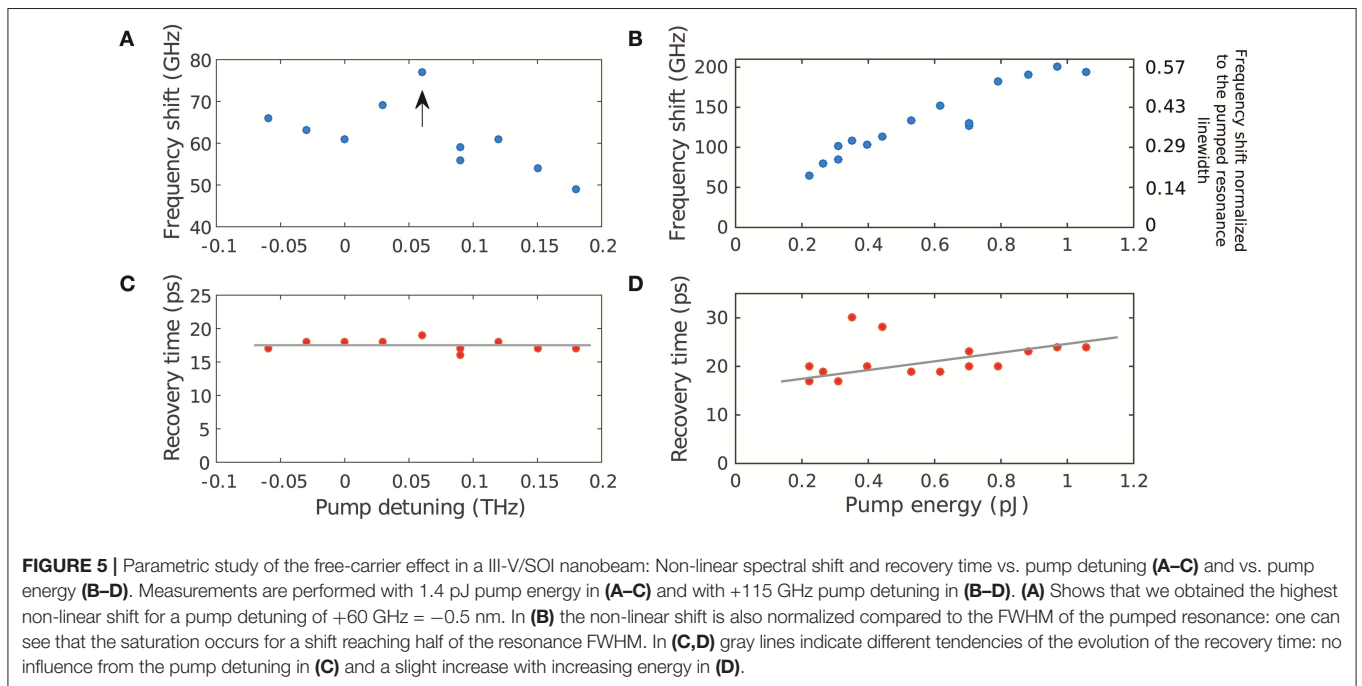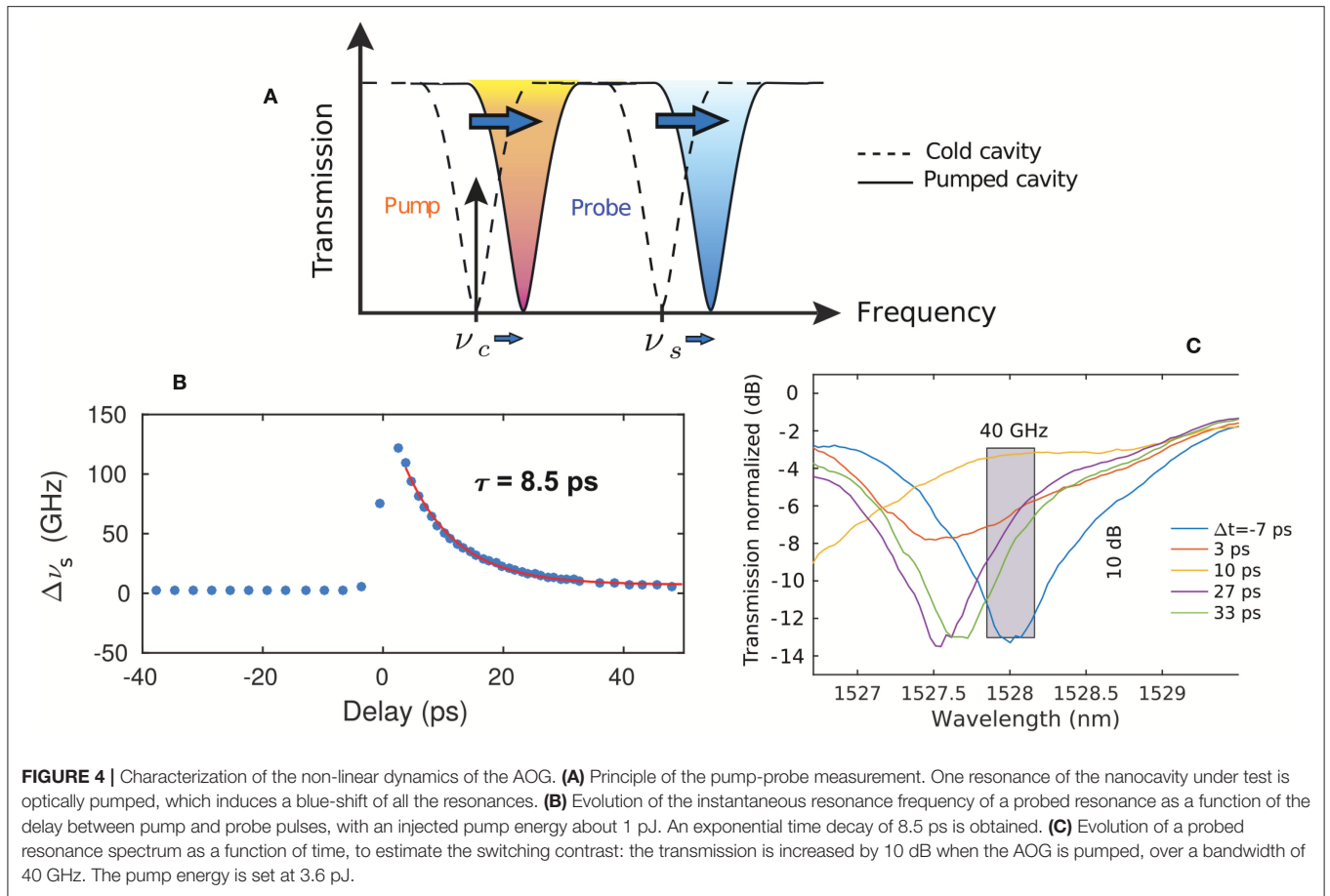
Based on the linear characterization, some properties of the non-linear dynamics of the AOG can be anticipated. First, the depth of each resonance indicates the maximum achievable switching contrast of the gate, thus between 8 and 15 dB in the sample studied above, and secondly the spectral linewidth $\Delta\lambda$ or FWHM (related to the loaded Q factor) directly affects the

FIGURE 3 | (A) Illustration and SEM photographies of our AOGs, consisting of InP PhC "nanobeam" bonded on a SOI circuitry. BCB, benzo-cyclo-buthene; intermediate polymer used for the adhesive bonding of the III–V on the SOI sample. **(B)** Output power from of a nanobeam InP cavity hybridized on 350 nm wide SOI waveguide, with a flat white source centered around 1,550 nm as light input. We can observe the parabolic transfer function of the grating couplers, as well as three resonances at 1,528, 1,549, and 1,569 nm.
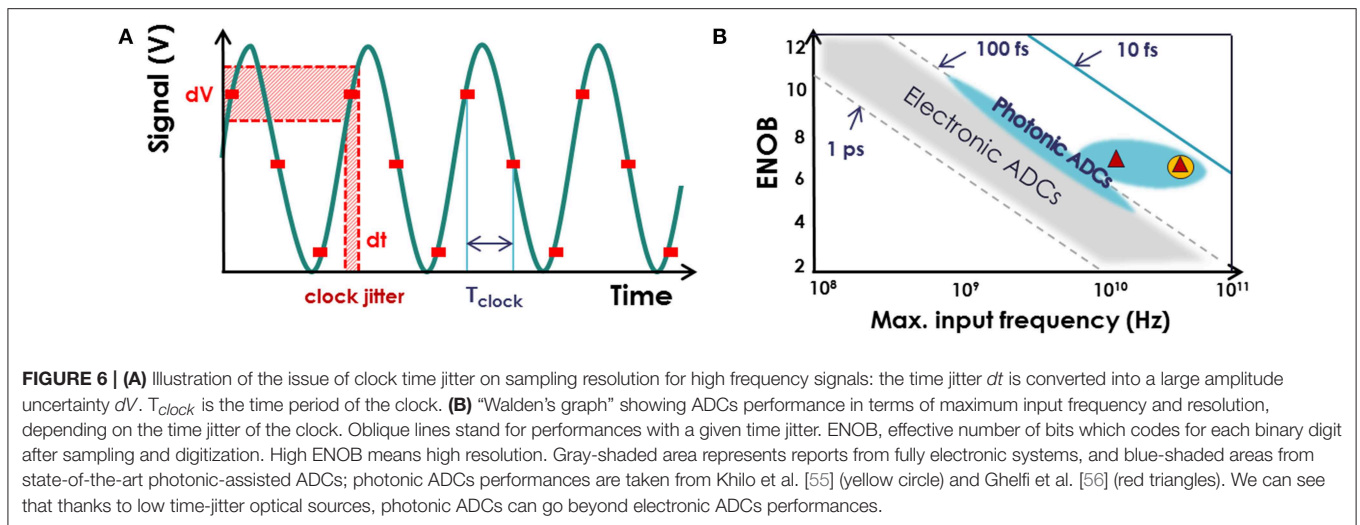
energy required for switching. Following these results, the time response of non-linear behavior of the gate was characterized through time-resolved pump-probe measurements. As shown in **Figure 4A**, the transmission spectrum of a resonator with at least two resonances is considered. While one mode is on resonance with the pump, the other resonance is probed with a broadband and short (< 1 ps) pulse, allowing the measurement of the time resolved transmission spectrum, from which the spectral shift is extracted. The procedure is detailed in Moille et al. [41]. An essential point here is that the spectral shift of the modes is identical. This condition is indeed well-satisfied as the two modes share approximately the same volume and overlap to the same population of excited free carriers. The pump pulses fed into the samples featured typically between 0.05 and 0.25 mW average power with a pulse duration of 6 ps and repetition rate 36 MHz, resulting in a peak power of 37 to 183 mW coupled into the waveguide, assuming coupling losses of 8dB. This corresponds to a switching energy from 0.22 to 1.1 pJ. The pulse duration was chosen to be close to the effective carrier lifetime to reach a trade-off between high non-linear effect and short recovery time [41]. The power in the probe was at least 2 orders of magnitude lower than the pump. Note that these pump powers values do not correspond to the dissipated power in the cavity, because only a fraction of the injected pump is absorbed in the cavity, thereby limiting heating in the nanostructure. Moreover, we would not be limited by thermal effects here, for the following reason: thermal effects are triggered by the pump absorbed inside the cavity, and the pump signal is periodic, with a time period much shorter than the typical thermal relaxation time (1 μs). This implies that the thermal effect remains constant in time, resulting only in an offset of temperature in the system leading to a fixed thermal spectral shift of the resonances, easily compensated. **Figure 4B** represents the typical response of the nanobeam AOGs during the pump-probe measurement, namely the instantaneous spectral shift of the probed resonance as a function of the pump-probe delay. A few picoseconds after the excitation, the resonance exhibits a fast (determined here by the pump pulse

duration) blue-shift reaching 120 GHz (−0.96 nm), followed by a slower relaxation which is very well-fitted by a single exponential with a time constant of 8.5 ps. Note that the precision of the frequency shift is given by the resolution of the optical spectrum analyzer used to measure the spectra for each time delay, which is 5 GHz. This time-resolved spectral measurement gives insight on the switching capabilities of the gate: **Figure 4C** shows that the transmission lineshape is essentially blue-shifted with minor distortion. More importantly, the 10 dB depth of the resonance is retrieved here as a transmission contrast of 10 dB, over a spectral width of at least 40 GHz. This large operation bandwidth is important when processing a signal, to avoid signal distortion when passing through the AOG. It is worth comparing with earlier measurements on III-V/Si hybrid gates [22], and we note that the recovery time may change by a factor two. This indicates that surface recombination critically depends on the properties of the InGaAs layer, which might vary from one fabrication batch to another. This stabilization issue should be resolved in a future industrialization phase with manufacturing clean room facilities.

The non-linear process is essentially dominated by the switching energy and the detuning of the pump. Indeed, a slight blue detuning of the pump improves the power transfer to the cavity as the resonance starts to be blue-shifted [53]. Accordingly, pump-probe measurements were performed with a range of pump wavelengths around the pumped resonance to find the optimum pump detuning. The results are reported in **Figure 5A**, note that they pertain to a different sample than the results shown in **Figure 4**. As expected we observed an influence of the pump detuning on the frequency shift, and the optimum pump detuning seems to be around +60 GHz (−0.5 nm), which is consistent with previous experiments [41, 53]. However there does not seem to be an influence on the recovery time, as shown in **Figure 5C**. Assuming that the fluctuations of the response time come from measurement uncertainties, we derived the latter by calculating the standard deviation of values reported in **Figure 5C** and found it to be close to 1 ps. Increasing the switching energy induces also

FIGURE 4 | Characterization of the non-linear dynamics of the AOG. **(A)** Principle of the pump-probe measurement. One resonance of the nanocavity under test is optically pumped, which induces a blue-shift of all the resonances. **(B)** Evolution of the instantaneous resonance frequency of a probed resonance as a function of the delay between pump and probe pulses, with an injected pump energy about 1 pJ. An exponential time decay of 8.5 ps is obtained. **(C)** Evolution of a probed resonance spectrum as a function of time, to estimate the switching contrast: the transmission is increased by 10 dB when the AOG is pumped, over a bandwidth of 40 GHz. The pump energy is set at 3.6 pJ.

FIGURE 5 | Parametric study of the free-carrier effect in a III-V/SOI nanobeam: Non-linear spectral shift and recovery time vs. pump detuning **(A–C)** and vs. pump energy **(B–D)**. Measurements are performed with 1.4 pJ pump energy in **(A–C)** and with +115 GHz pump detuning in **(B–D)**. **(A)** Shows that we obtained the highest non-linear shift for a pump detuning of +60 GHz = −0.5 nm. In **(B)** the non-linear shift is also normalized compared to the FWHM of the pumped resonance: one can see that the saturation occurs for a shift reaching half of the resonance FWHM. In **(C,D)** gray lines indicate different tendencies of the evolution of the recovery time: no influence from the pump detuning in **(C)** and a slight increase with increasing energy in **(D)**.

FIGURE 6 | (A) Illustration of the issue of clock time jitter on sampling resolution for high frequency signals: the time jitter *dt* is converted into a large amplitude uncertainty *dV*. T_{clock} is the time period of the clock. **(B)** "Walden's graph" showing ADCs performance in terms of maximum input frequency and resolution, depending on the time jitter of the clock. Oblique lines stand for performances with a given time jitter. ENOB, effective number of bits which codes for each binary digit after sampling and digitization. High ENOB means high resolution. Gray-shaded area represents reports from fully electronic systems, and blue-shaded areas from state-of-the-art photonic-assisted ADCs; photonic ADCs performances are taken from Khilo et al. [55] (yellow circle) and Ghelfi et al. [56] (red triangles). We can see that thanks to low time-jitter optical sources, photonic ADCs can go beyond electronic ADCs performances.

interesting behaviors on the non-linear process: in **Figure 5B**, one can see a linear behavior as a function of the pump energy, up to a saturation level when reaching about 1.1 pJ and a non-linear shift of 200 GHz (−1.6 nm). This saturation is due to the fact that the more pump power is injected, the further the pumped resonance is shifted by FCD, thereby reducing the amount of light coupled into the cavity. This goes on until higher powers do not compensate the decreasing coupling, resulting in a saturating non-linear shift. This is consistent with the fact that the saturation occurs when the resonances are shifted by more than half the FWHM of the pumped resonance, as it can be seen in **Figure 5B**. We note that chirped pulses may considerably extend the blue shift, as demonstrated in Serna et al. [54]. Finally, as shown in **Figure 5D** we observed a slight increase of the recovery time when increasing the switching energy. This is likely due to a saturation of the surface recombination process when many carriers are generated due to a high pump power, which slows down the relaxation of the free-carrier effect.

Based on these results it is concluded that the hybrid III–V/Si AOGs technology is comparable in performance to other AOGs, which is apparent in **Figure 2**. Energy efficiency could however be improved by playing with the material non-linearity like in Nozaki et al. [19], or with the design of the cavity by using Fano cavities like in Yu et al. [40]. Nonetheless all-optical processing with signals up to several tens of GHz are possible, consistently with earlier experiments [19, 39, 53]. Importantly, this comes with an integrated photonic platform, thereby considerably extending the capabilities for a broad range of applications.
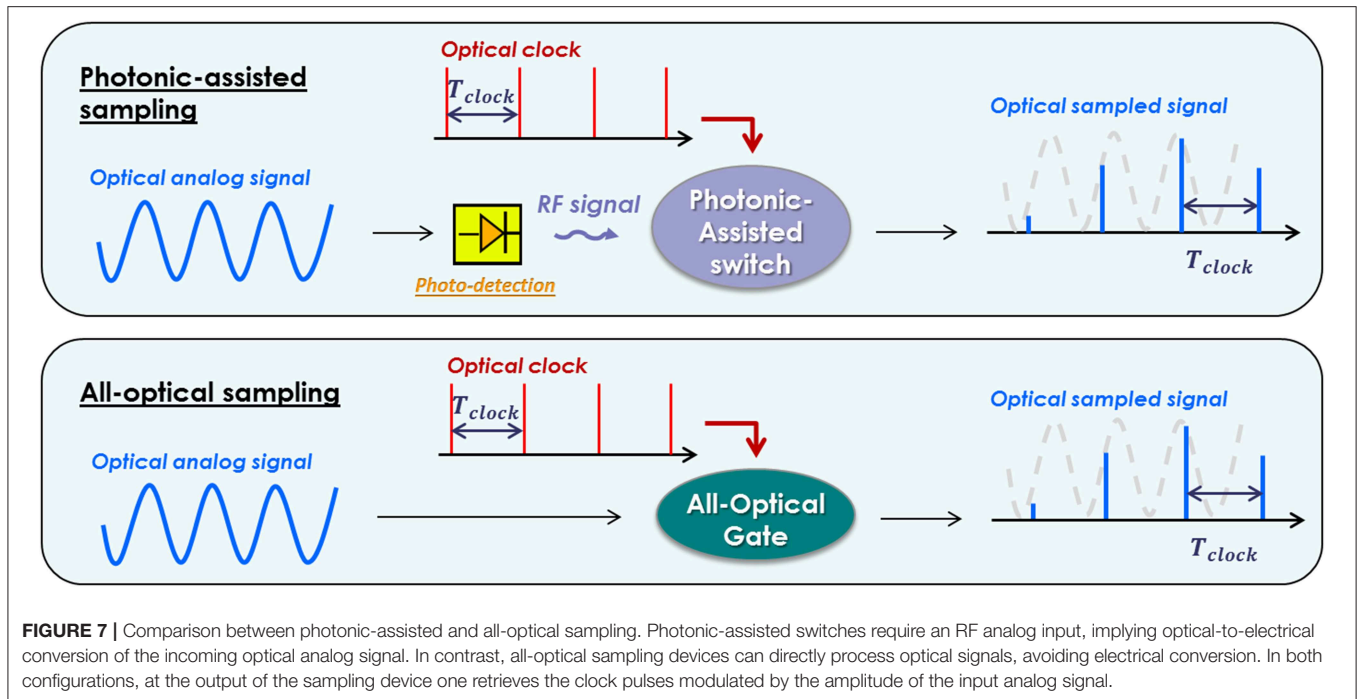
4. ALL-OPTICAL SAMPLING WITH III–V/SI ALL-OPTICAL GATES

4.1. Photonic Analog-to-Digital Conversion

Sampling, through which a modulated analog signal is converted into a discontinuous analog signal, is a substantial part of the analog-to-digital (A/D) conversion process. The latter is constantly present in daily life or in research and industry labs

when using devices or instruments relying on the acquisition of analog signals like sounds, images or any physical signal. As an example, in the context of radars or wideband radio communications, signals have a narrow spectrum around a high frequency carrier (10–100 GHz), and the A/D conversion is performed after demodulation to the baseband. It would be simpler to digitize directly on the high frequency signal, implying available A/D converters (ADCs) operating at high frequencies. But, as illustrated in **Figure 6A**, the inherent difficulty when sampling a high-speed signal lies on the fact that a small time error of the clock (periodic signal which gives the sampling instants) results in a high amplitude uncertainty on the sampled signal, limiting the resolution. This time error is called the time jitter, and electronic clocks exhibit time jitters of at least 60 fs [57]. As a consequence, electronic ADCs can hardly process signals of several tens of GHz with a sufficiently high resolution, as shown in **Figure 6B**. The use of low-time-jitter optical sources, like mode-locked lasers featuring down to subfemtosecond jitter [58], would remove the electronic ADCs bottleneck and the sampling rate could be increased without inherent resolution loss [37]. This defines the concept of photonic-assisted ADCs, where for example a low-time-jitter optical pulse train (the clock) is modulated by an RF input (the signal to be sampled) before being digitized [55, 59].

Now, following the advances in the development of all-optical signal processing devices and optical data links, it seems logical that all-optical A/D conversion, or at least all-optical sampling, with both the clock and the signal in the optical domain, should also be implemented, in order to directly convert optical signals without preliminary optical-to-electrical conversion, as illustrated in **Figure 7**. Thus, AOGs are essential elements to create all-optical sampling devices, with the clock being the control signal which activates the gate to sample the incoming optical signal, as shown in **Figure 7**. The performance criteria for all-optical sampling devices are the maximum input frequency, and the resolution: both criteria are complementary and form a figure of merit whose limiting factor is the time jitter of the clock, which is illustrated in "Walden's graph" in **Figure 6B**.

FIGURE 7 | Comparison between photonic-assisted and all-optical sampling. Photonic-assisted switches require an RF analog input, implying optical-to-electrical conversion of the incoming optical analog signal. In contrast, all-optical sampling devices can directly process optical signals, avoiding electrical conversion. In both configurations, at the output of the sampling device one retrieves the clock pulses modulated by the amplitude of the input analog signal.

In the following subsection we describe our all-optical sampling experiment using our hybrid III-V/SOI PhC-based AOGs, as briefly described in Constans et al. [60].

4.2. All-Optical Sampling Experiment via III–V/SOI PhC-Based AOG

The performance criteria of an AOG as an all-optical sampling device are:

1. the switching contrast or transmission contrast, which impacts the resolution of the sampled signal,
2. the response time, which limits the maximum input frequency, and
3. the switching energy, here the energy sent to the AOG at each clock pulse, also the energy needed to generate one sample, expressed in Joule per sample or J/bit.
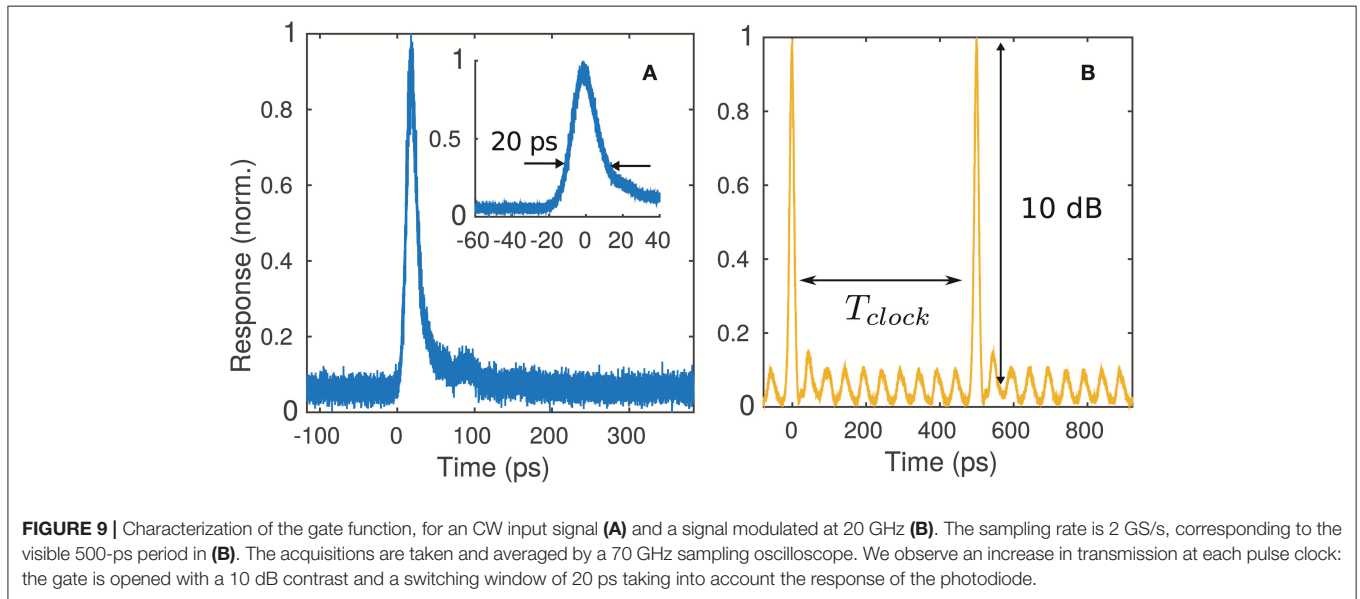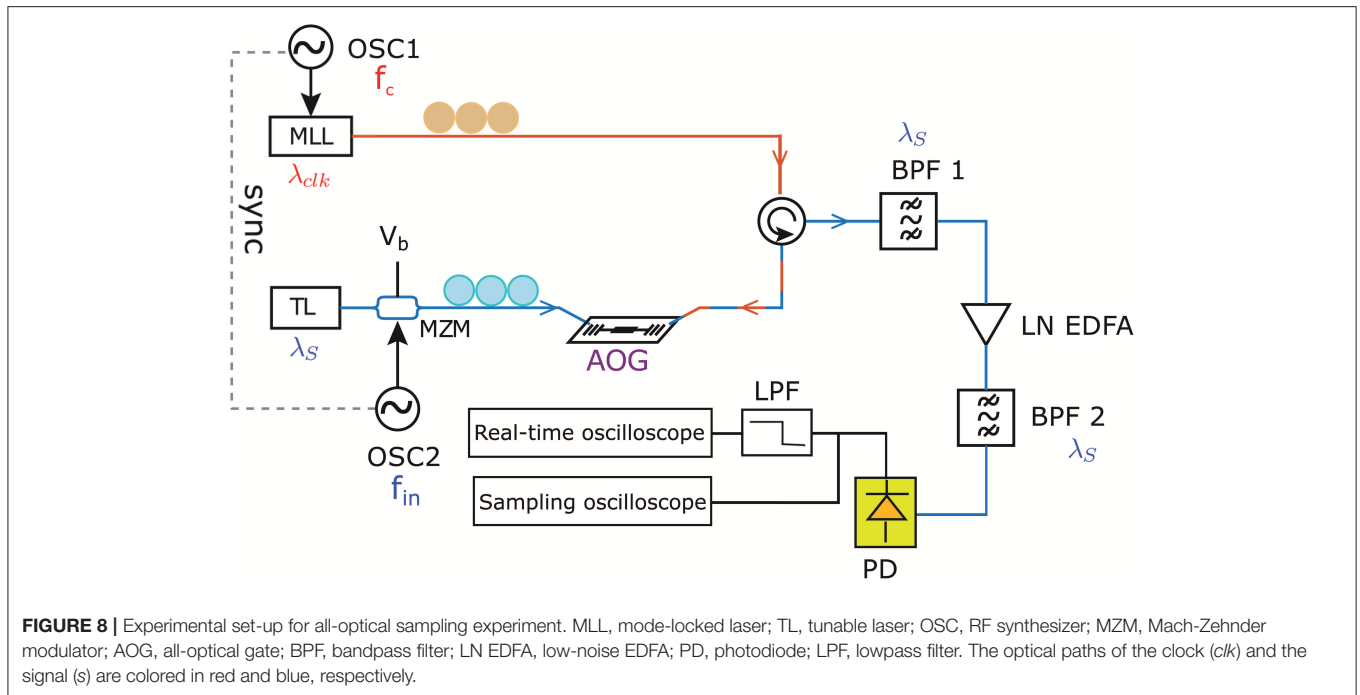
As the maximum frequency which can be resolved is related to the switching window ($\Delta t \approx 8$–20 ps at a few 100s fJ switching energies, as measured during the pump-probe experiments described in the previous section), with our fast PhC-based AOGs the expected limit here close to 50 GHz, but could possibly extend to 100 GHz. We note that a short burst of pulses separated by 10 ps has been resolved during our sampling experiment using a PhC non-linear gate [41].

In order to demonstrate the sampling performances of our AOGs we performed all-optical sampling measurements at a sampling rate of 2 GS/s (samples/second) with the experimental set-up shown in **Figure 8**. The 2 GHz clock signal (f_c) is generated by a tunable actively mode-locked laser driven by a RF synthesizer. The optical signal to be sampled is a CW signal from a tunable laser modulated by a Mach-Zehnder modulator which is driven by a second RF synthesizer, synchronized to the first one.

The corresponding input frequencies f_{in} range from 2 to 40 GHz. In contrast to the pump-probe experiments, here both signal (λ_s) and clock (λ_c) spectrally match a resonance of the cavity. Signal and clock are sent to the AOG in a counter-propagative configuration: the clock is fed into the AOG by a circulator which at the same time extracts the sampled signal transmitted by the AOG. This avoids interaction between the clock and the signal in the fibers before the AOG. Then an optical bandpass filter is used to extract the sampled signal from the residual clock. The sampled signal is finally amplified with a low-noise EDFA, and again filtered to reject the amplifier noise. We used of fast photodiode (40 GHz) to detect the samples and send them to an oscilloscope.

The parameters of the AOG are 10 dB-deep resonances featuring 15 ps recovery times. The clock source and the amplifier were set to obtain 8 ps pump pulses and an average power of 9 mW at the input of the fiber which couples the light to the grating couplers. This means about 90 mW peak power and 0.7 pJ/bit coupled into the AOG waveguide. Before the sampling experiment, we characterized the gate function of the AOG with a fast sampling oscilloscope (70 GHz), for a CW signal and for a signal modulated at 20 GHz. The results are shown in **Figure 9**. We measured a switching window of <20 ps taking into account the response of the photodiode (about 10 ps), and a switching contrast of 10 dB, consistently with pump-probe measurements.

We next assessed the sampling capability of the AOG, by sampling and reconstructing known sinusoidal optical signals at frequencies from 8 to 38 GHz. To do so, the optical samples were acquired in the baseband after photodetection and lowpass filtering. The acquisition was performed by a digital real-time oscilloscope. In order to extract the signal-to-noise ratio (SNR),
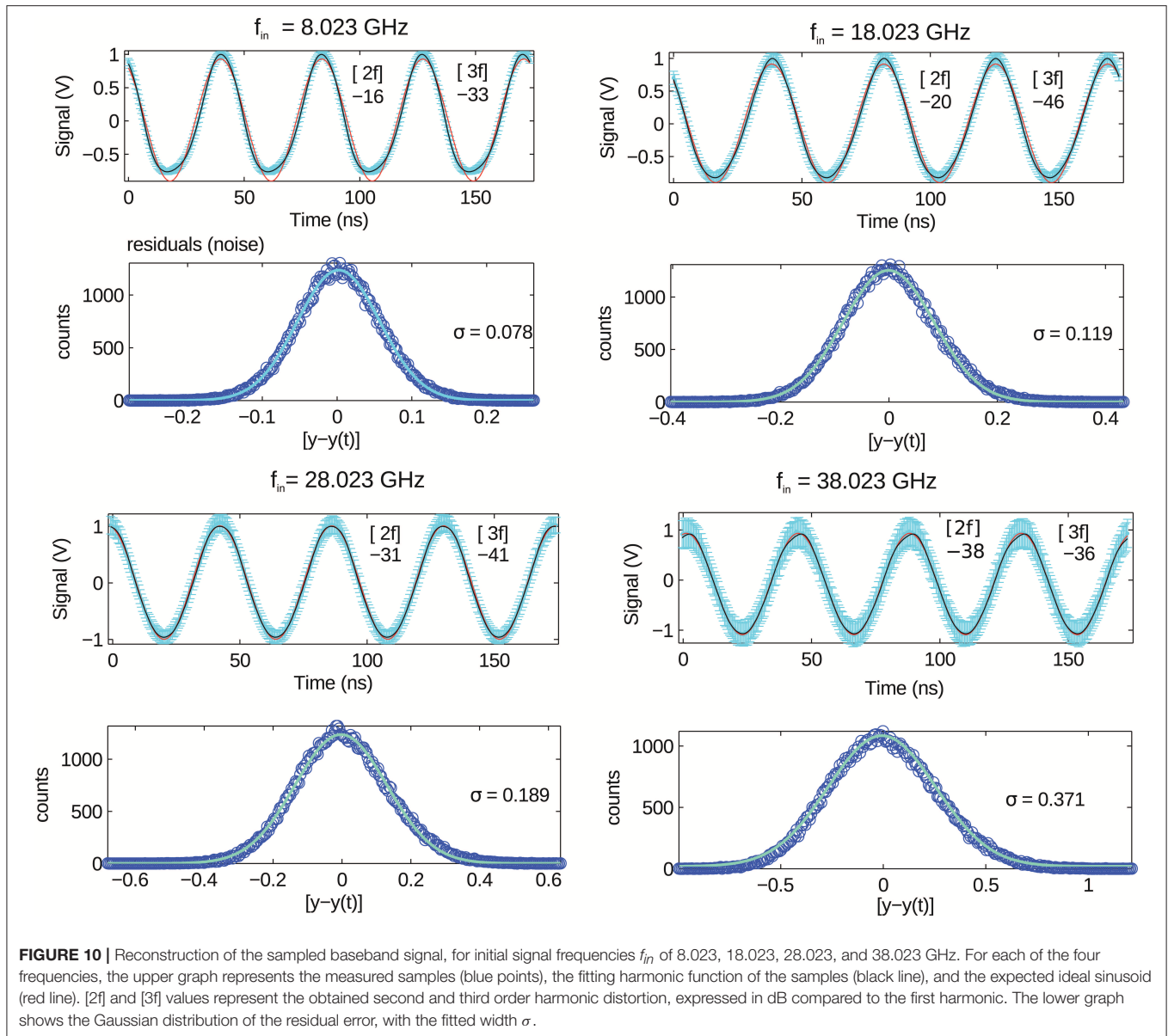
FIGURE 8 | Experimental set-up for all-optical sampling experiment. MLL, mode-locked laser; TL, tunable laser; OSC, RF synthesizer; MZM, Mach-Zehnder modulator; AOG, all-optical gate; BPF, bandpass filter; LN EDFA, low-noise EDFA; PD, photodiode; LPF, lowpass filter. The optical paths of the clock (clk) and the signal (s) are colored in red and blue, respectively.

FIGURE 9 | Characterization of the gate function, for an CW input signal **(A)** and a signal modulated at 20 GHz **(B)**. The sampling rate is 2 GS/s, corresponding to the visible 500-ps period in **(B)**. The acquisitions are taken and averaged by a 70 GHz sampling oscilloscope. We observe an increase in transmission at each pulse clock: the gate is opened with a 10 dB contrast and a switching window of 20 ps taking into account the response of the photodiode.

the acquired samples were folded over four periods of the baseband signal as shown in **Figure 10**, and the samples were fitted by an harmonic function. By comparing this fitting function to an ideal sinusoid, we obtained the SNR as well as the harmonic distortion.

By inspecting the plots of the measured samples for different input frequencies in **Figure 10**, it is noted that the noise increases for increasing frequencies, leading to a SNR decreasing from 28 to 15 dB. In contrast, harmonic distortion decreases with increasing frequencies. A comparison with recent literature considers all-optical sampling based on FWM in a 12-meter long

highly non-linear fiber, achieving digitization of as high as 100 GHz optical signal at a 10 GS/s sampling rate, with an effective resolution of 6 ENOB (Effective Number Of Bits, see **Figure 6B**), corresponding to SNR = 36 dB [61]. The larger bandwidth and sampling rate and better resolution are achieved at the cost of a substantially larger energy of 52 pJ/bit (2 orders of magnitude) and a large footprint, but illustrate the performance potential of all-optical techniques, where the key is the miniaturization.

The future integration of the whole sampling circuit, including the optical sources, the combiners to combine both inputs, and the filters to isolate the signal, will highly reduce insertion
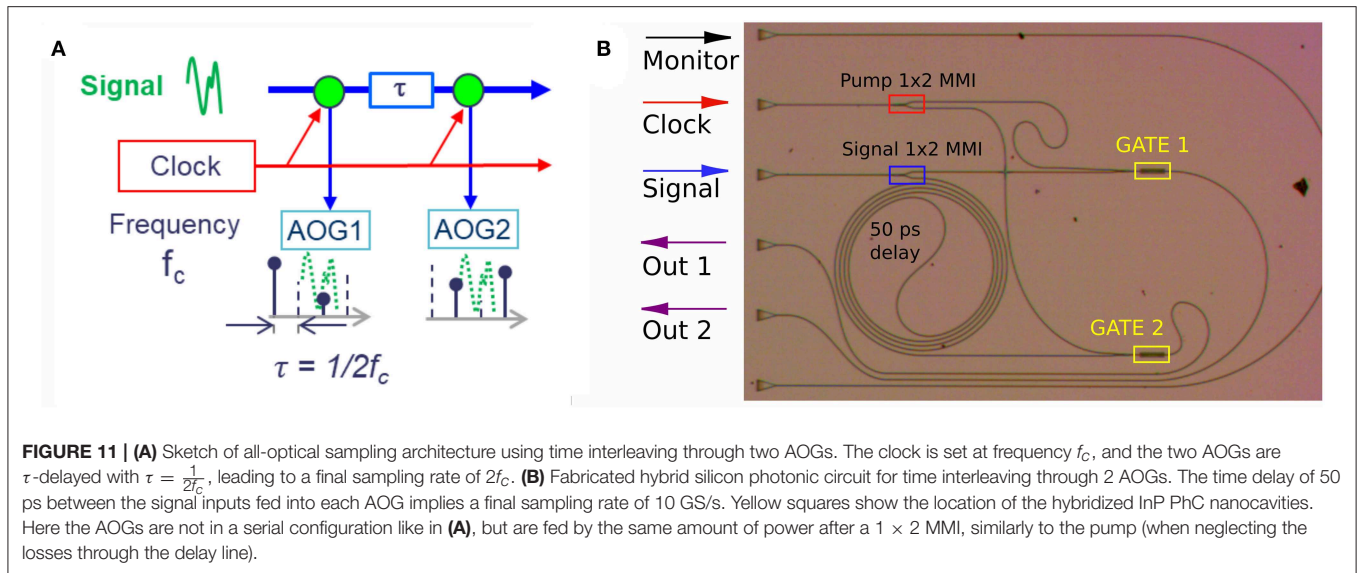
FIGURE 10 | Reconstruction of the sampled baseband signal, for initial signal frequencies f_{in} of 8.023, 18.023, 28.023, and 38.023 GHz. For each of the four frequencies, the upper graph represents the measured samples (blue points), the fitting harmonic function of the samples (black line), and the expected ideal sinusoid (red line). [2f] and [3f] values represent the obtained second and third order harmonic distortion, expressed in dB compared to the first harmonic. The lower graph shows the Gaussian distribution of the residual error, with the fitted width σ.

losses and the need for further amplification, thus improving the SNR and the resolution of the sampling process. Besides this leads to the implementation of more complex integrated sampling architectures, like multichannel sampling in order to increase the final sampling rate, as it is described in the following section.

5. CONCLUSION AND OUTLOOK: INTEGRATED NON-LINEAR ALL-OPTICAL PROCESSING

The manufacturing capabilities of the CMOS foundries used for silicon photonics enable complex integrated photonic architectures, which have been used for optical signal processing [55, 56, 62, 63], optical computing [4, 5], and quantum optics where integration enables high precision and controllability [64]. In contrast, the demonstration of photonic integrated architectures for all-optical signal processing are more challenging and only a few approaches seem to have reached the scale of a non-linear integrated circuit [65–69].

Relying on the higher non-linearity of III–V semiconductor alloys, the hybrid III–V/Si technology turns out highly relevant to provide non-linear elements that can fit in already existing silicon photonic architectures. Combined to the low footprint and the energy efficiency displayed by fast hybrid PhC-based AOGs, this opens the perspective of building scalable and low-power-consuming integrated silicon photonic circuits including fast non-linear functions, leading to high-performance all-optical signal processing, such as optical pulse shaping,

FIGURE 11 | (A) Sketch of all-optical sampling architecture using time interleaving through two AOGs. The clock is set at frequency f_C, and the two AOGs are τ-delayed with $\tau = \frac{1}{2f_C}$, leading to a final sampling rate of $2f_C$. **(B)** Fabricated hybrid silicon photonic circuit for time interleaving through 2 AOGs. The time delay of 50 ps between the signal inputs fed into each AOG implies a final sampling rate of 10 GS/s. Yellow squares show the location of the hybridized InP PhC nanocavities. Here the AOGs are not in a serial configuration like in **(A)**, but are fed by the same amount of power after a 1×2 MMI, similarly to the pump (when neglecting the losses through the delay line).

optical time-division multiplexing. In this perspective, an integrated silicon photonic circuit with two hybrid AOGs has been developed. This architecture is meant to perform all-optical sampling through time interleaving. Interleaving techniques enable to scale the sampling rate up, while keeping the same clock frequency [70]. In wavelength-interleaved systems, consecutive sampling pulses have different central wavelengths, and the corresponding samples can be switched to different outputs using a wavelength demultiplexer [62]. In time-interleaved devices, as illustrated in **Figure 11A**, each sampling gate sees the signal to be sampled with a different time delay, obtaining as many samples in a single period of the clock (with one different output for each gate). In other words a fast serial input pulse train is converted into multiple parallel lower-rate pulse trains. The integrated approach for time-interleaving enables to avoid the issue of the synchronization of the clock pulses toward each gate, which is easily controlled by adjusting the length of each path.

The hybrid silicon photonic circuit fabricated to perform time interleaving is shown in **Figure 11B**. The mastery and flexibility of silicon photonics allow to build this circuit using splitters and combiners, time delay lines and crossings (mandatory for this architecture implemented in 2D), resulting in an architecture rather simple compared to time interleaved electronic ADCs [71]. Both the signal to be sampled and the control signal (control pulses) are splitted and distributed with the same amount of power to the different gates, here two gates, via multimode interferometers (MMIs), as shown in **Figure 11B**. So the injected total switching energy scales with the number of gates of the circuits. Here the signal is fed into the two gates with a 50 ps delay between the gates, meaning that the clock has a time period of 100 ps, or 10 GHz repetition rate. The two pump paths are optimized to have the same length and the same propagation time within 100 fs to ensure the simultaneous activation of both AOGs.

This work contributes to the transition from non-linear photonic devices to non-linear photonic circuits. By combining the advantages of silicon photonics with high performance AOGs, this technology is relevant to a very broad range of applications, well-beyond all-optical sampling. In particular, they could implement an ultra-fast and energy efficient non-linear activation function which is an essential ingredient of photonic neural networks [4].

DATA AVAILABILITY

The datasets generated for this study are available on request to the corresponding author.

AUTHOR CONTRIBUTIONS

For the original results of this article, the III–V epitaxies were fabricated by GB and IS. The design of the nanocavities were designed by FR and LC, and the silicon photonic sampling circuits by AR and SC. The fabrication process for the III–V/Si samples and the silicon circuits owe to the contribution of FR, XC, and LC. All measurements were performed by AR, SC, and LC.

FUNDING

ACKNOWLEDGMENTS

REFERENCES

1. Mittal S. A survey of techniques for improving energy efficiency in embedded computing systems. *arXiv[Preprint].arXiv:1401.0765.* (2013). doi: 10.1504/IJCAET.2014.065419

2. Miller DA. Device requirements for optical interconnects to silicon chips. *Proc IEEE.* (2009) **97**:1166–85. doi: 10.1109/JPROC.2009.2014298

3. Rumley S, Bahadori M, Polster R, Hammond SD, Calhoun DM, Wen K, et al. Optical interconnects for extreme scale computing systems. *Parallel Comput.* (2017) **64**:65–80. doi: 10.1016/j.parco.2017.02.001

4. Shen Y, Harris NC, Skirlo S, Prabhu M, Baehr-Jones T, Hochberg M, et al. Deep learning with coherent nanophotonic circuits. *Nat Photon.* (2017) **11**:441. doi: 10.1038/nphoton.2017.93

5. Vandoorne K, Mechet P, Van Vaerenbergh T, Fiers M, Morthier G, Verstraeten D, et al. Experimental demonstration of reservoir computing on a silicon photonics chip. *Nat Commun.* (2014) **5**:3541. doi: 10.1038/ncomms4541

6. Duport F, Schneider B, Smerieri A, Haelterman M, Massar S. All-optical reservoir computing. *Opt Express.* (2012) **20**:22783–95. doi: 10.1364/OE.20.022783

7. Dorren H, Hill M, Liu Y, Calabretta N, Srivatsa A, Huijskens F, et al. Optical packet switching and buffering by using all-optical signal processing methods. *J Lightw Technol.* (2003) **21**:2. doi: 10.1109/JLT.2002.803062

8. Doran N, Wood D. Nonlinear-optical loop mirror. *Opt Lett.* (1988) **13**:56–8.

9. Diez S, Schmidt C, Ludwig R, Weber HG, Obermann K, Kindt S, et al. Four-wave mixing in semiconductor optical amplifiers for frequency conversion and fast optical switching. *IEEE J Select Top Quantum Electron.* (1997) **3**:1131–45.

10. Bilenca A, Alizon R, Mikhelashhvili V, Dahan D, Eisenstein G, Schwertberger R, et al. Broad-band wavelength conversion based on cross-gain modulation and four-wave mixing in InAs-InP quantum-dash semiconductor optical amplifiers operating at 1550 nm. *IEEE Photon Technol Lett.* (2003) **15**:563–5. doi: 10.1109/LPT.2003.809281

11. Van V, Ibrahim TA, Absil PP, Johnson FG, Grover R, Ho PT. Optical signal processing using nonlinear semiconductor microring resonators. *IEEE J Select Top Quantum Electron.* (2002) **8**:705–13. doi: 10.1109/JSTQE.2002.1016376

12. Lipson M. Overcoming the limitations of microelectronics using Si nanophotonics: solving the coupling, modulation and switching challenges. *Nanotechnology.* (2004) **15**:S622–7. doi: 10.1088/0957-4484/15/10/020

13. John S. Strong localization of photons in certain disordered dielectric superlattices. *Phys Rev Lett.* (1987) **58**:2486.

14. Zhang Z, Qiu M. Small-volume waveguide-section high Q microcavities in 2D photonic crystal slabs. *Opt Express.* (2004) **12**:3988–95. doi: 10.1364/opex.12.003988

15. Asano T, Ochi Y, Takahashi Y, Kishimoto K, Noda S. Photonic crystal nanocavity with a Q factor exceeding eleven million. *Opt Express.* (2017) **25**:1769–77. doi: 10.1364/OE.25.001769

16. Tanabe T, Notomi M, Mitsugi S, Shinya A, Kuramochi E. All-optical switches on a silicon chip realized using photonic crystal nanocavities. *Appl Phys Lett.* (2005) **87**:151112. doi: 10.1063/1.2089185

17. Bristow AD, Astratov VN, Shimada R, Culshaw IS, Skolnick MS, Whittaker DM, et al. Polarization conversion in the reflectivity properties of photonic crystal waveguides. *IEEE J Quantum Electron.* (2002) **38**:880–4. doi: 10.1109/JQE.2002.1017601

18. Husko C, De Rossi A, Combri S, Tran QV, Raineri F, Wong CW. Ultrafast all-optical modulation in GaAs photonic crystal cavities. *Appl Phys Lett.* (2009) **94**:021111. doi: 10.1063/1.3068755

19. Nozaki K, Tanabe T, Shinya A, Matsuo S, Sato T, Taniyama H, et al. Sub-femtojoule all-optical switching using a photonic-crystal nanocavity. *Nat Photon.* (2010) **4**:477–83. doi: 10.1038/nphoton.2010.89

20. Roelkens G, Abassi A, Cardile P, Dave U, de Groote A, de Koninck Y, et al. III-V-on-silicon photonic devices for optical communication and sensing. *Photonics.* (2015) **2**:969–1004. doi: 10.3390/photonics2030969

21. Crosnier G, Sanchez D, Bouchoule S, Monnier P, Beaudoin G, Sagnes I, et al. Hybrid indium phosphide-on-silicon nanolaser diode. *Nat Photon.* (2017) **11**:297–300. doi: 10.1038/nphoton.2017.56

22. Bazin A, Lenglé K, Gay M, Monnier P, Bramerie L, Braive R, et al. Ultrafast all-optical switching and error-free 10 Gbit/s wavelength conversion in hybrid

InP-silicon on insulator nanocavities using surface quantum wells. *Appl Phys Lett.* (2014) **104**:011102. doi: 10.1063/1.4861121

23. Bennett BR, Soref RA, del Alamo JA. Carrier-induced change in refractive index of InP, GaAs and InGaAsP. *IEEE J Quantum Electron.* (1990) **26**:113–22.

24. Moille G. *Non-Linear Dynamics in Semiconductor Nano-Structures for Signal Processing.* Palaiseau: Université Paris Saclay (2016).

25. Nakamura S, Ueno Y, Tajima K. Femtosecond switching with semiconductor-optical-amplifier-based Symmetric Mach–Zehnder-type all-optical switch. *Appl Phys Lett.* (2001) **78**:3929. doi: 10.1063/1.1379790

26. Schreieck RP, Kwakernaak MH, Jackel H, Melchior H. All-optical switching at multi-100-Gb/s data rates with Mach-Zehnder interferometer switches. *IEEE J Quantum Electron.* (2002) **38**:1053–61. doi: 10.1109/JQE.2002.800994

27. Ju H, Zhang S, Lenstra D, De Waardt H, Tangdiongga E, Khoe GD, et al. SOA-based all-optical switch with subpicosecond full recovery. *Opt Express.* (2005) **13**:942–7. doi: 10.1364/OPEX.13.000942

28. Koos C, Vorreau P, Vallaitis T, Dumon P, Bogaerts W, Baets R, et al. All-optical high-speed signal processing with silicon–organic hybrid slot waveguides. *Nat Photon.* (2009) **3**:216–9. doi: 10.1038/nphoton.2009.25

29. Yüce E, Ctistis G, Claudon J, Dupuy E, Buijs RD, de Ronde B, et al. All-optical switching of a microcavity repeated at terahertz rates. *Opt Lett.* (2013) **38**:374. doi: 10.1364/OL.38.000374

30. Constans L, Marty G, Combrié S, Sanchez D, Raineri F, de Rossi A. All-optical sampling of a 40 GHz signal based on four wave-mixing through a nonlinear InGaP on Silicon platform. In: *CLEO Europe* Munich. (2019).

31. Cong GW, Akimoto R, Akita K, Hasama T, Ishikawa H. Low-saturation-energy-driven ultrafast all-optical switching operation in (CdS/ZnSe)/BeTe intersubband transition. *Opt Express.* (2007) **15**:12123–30. doi: 10.1364/OE.15.012123

32. Akimoto R, Gozu S, Mozume T, Ishikawa H. Monolithically integrated all-optical gate switch using intersubband transition in InGaAs/AlAsSb coupled double quantum wells. *Opt Express.* (2011) **19**:13386–94. doi: 10.1364/OE.19.013386

33. Monteagudo-Lerma L, Valdueza-Felip S, Naranjo FB, Corredera P, Rapenne L, Sarigiannidou E, et al. Waveguide saturable absorbers at 1.55 μm based on intraband transitions in GaN/AlN QDs. *Opt Express.* (2013) **21**:27578–86. doi: 10.1364/oe.21.027578

34. Ibrahim TA, Van V, Ho PT. All-optical time-division demultiplexing and spatial pulse routing with a GaAs/AlGaAs microring resonator. *Opt Lett.* (2002) **27**:803–805. doi: 10.1364/ol.27.000803

35. Ibrahim TA, Grover R, Kuo LC, Kanakaraju S, Calhoun LC, Ho PT. All-optical AND/NAND logic gates using semiconductor microresonators. *IEEE Photon Technol Lett.* (2003) **15**:1422–4. doi: 10.1109/LPT.2003.818049

36. Almeida VR, Barrios CA, Panepucci RR, Lipson M. All-optical control of light on a silicon chip. *Nature.* (2004) **431**:1081–4. doi: 10.1038/nature02921

37. Waldow M, Plötzing T, Gottheil M, Först M, Bolten J, Wahlbrink T, et al. 25ps all-optical switching in oxygen implanted silicon-on-insulator microring resonator. *Opt Express.* (2008) **16**:7693. doi: 10.1364/OE.16.007693

38. Tanabe T, Nishiguchi K, Shinya A, Kuramochi E, Inokawa H, Notomi M, et al. Fast all-optical switching using ion-implanted silicon photonic crystal nanocavities. *Appl Phys Lett.* (2007) **90**:031115. doi: 10.1063/1.2431767

39. Combrié S, Lehoucq G, Junay A, Malaguti S, Bellanca G, Trillo S, et al. All-optical signal processing at 10 GHz using a photonic crystal molecule. *Appl Phys Lett.* (2013) **103**:193510. doi: 10.1063/1.4829556

40. Yu Y, Hu H, Oxenløwe LK, Yvind K, Mork J. Ultrafast all-optical modulation using a photonic-crystal Fano structure with broken symmetry. *Opt Lett.* (2015) **40**:2357. doi: 10.1364/OL.40.002357

41. Moille G, Combrié S, Morgenroth L, Lehoucq G, Neuilly F, Hu B, et al. Integrated all-optical switch with 10 ps time resolution enabled by ALD: integrated all-optical switch with 10 ps time. *Laser Photon Rev.* (2016) **10**:409–19. doi: 10.1002/lpor.201500197

42. Bazin A, Raj R, Raineri F. Design of silica encapsulated high-Q photonic crystal nanobeam cavity. *J Lightw Technol.* (2014) **32**:952–8. doi: 10.1109/JLT.2013.2295267

43. Shockley W. Holes and electrons. *Phys Today.* (1950) **3**:16.

44. Tanabe T, Taniyama H, Notomi M. Carrier diffusion and recombination in photonic crystal nanocavity optical switches. *J Lightw Technol.* (2008) **26**:1396–403. doi: 10.1109/JLT.2008.923638

45. Moille G, Combrié S, Fuchs K, Yacob M, Reithmaier JP, de Rossi A. Acceleration of the nonlinear dynamics in p-doped indium phosphide nanoscale resonators. *Opt Lett.* (2017) **42**:795–8. doi: 10.1364/OL.42.000795

46. Bekele DA, Yu Y, Hu H, Guan P, Galili M, Ottaviano L, et al. Signal reshaping and noise suppression using photonic crystal Fano structures. *Opt Express.* (2018) **26**:19596. doi: 10.1364/OE.26.019596

47. Liang D, Fang AW, Park H, Reynolds TE, Warner K, Oakley DC, et al. Low-temperature, strong SiO$_2$-SiO$_2$ covalent wafer bonding for III V compound semiconductors-to-silicon photonic integrated circuits. *J Electron Mater.* (2008) **37**:1552–9. doi: 10.1007/s11664-008-0489-1

48. Hiraki T, Aihara T, Hasebe K, Takeda K, Fujii T, Kakitsuka T, et al. Heterogeneously integrated III–V/Si MOS capacitor Mach–Zehnder modulator. *Nat Photon.* (2017) **11**:482. doi: 10.1038/nphoton.2017.120

49. Fitsios D, Alexoudi T, Bazin A, Monnier P, Raj R, Miliou A, et al. Ultra-compact III–V-on-Si photonic crystal memory for flip-flop operation at 5 Gb/s. *Opt Express.* (2016) **24**:4270–7. doi: 10.1364/OE.24.004270

50. Raineri F, Cojocaru C, Monnier P, Levenson A, Raj R, Seassal C, et al. Ultrafast dynamics of the third-order nonlinear response in a two-dimensional InP-based photonic crystal. *Appl Phys Lett.* (2004) **85**:1880. doi: 10.1063/1.1788884

51. Crosnier G, Sanchez D, Bazin A, Monnier P, Bouchoule S, Braive R, et al. High Q factor InP photonic crystal nanobeam cavities on silicon wire waveguides. *Opt Lett.* (2016) **41**:579. doi: 10.1364/OL.41.000579

52. Ashida K, Okano M, Ohtsuka M, Seki M, Yokoyama N, Koshino K, et al. Ultrahigh-Q photonic crystal nanocavities fabricated by CMOS process technologies. *Opt Express.* (2017) **25**:18165–74. doi: 10.1364/OE.25.018165

53. Lengle K, Nguyen TN, Gay M, Bramerie L, Simon JC, Bazin A, et al. Modulation contrast optimization for wavelength conversion of a 20 Gbit/s data signal in hybrid InP/SOI photonic crystal nanocavity. *Opt Lett.* (2014) **39**:2298. doi: 10.1364/OL.39.002298

54. Serna S, Oden J, Hanna M, Caer C, Le Roux X, Sauvan C, et al. Enhanced nonlinear interaction in a microcavity under coherent excitation. *Opt Express.* (2015) **23**:29964–77. doi: 10.1364/OE.23.029964

55. Khilo A, Spector SJ, Grein ME, Nejadmalayeri AH, Holzwarth CW, Sander MY, et al. Photonic ADC: overcoming the bottleneck of electronic jitter. *Opt Express.* (2012) **20**:4454–69. doi: 10.1364/OE.20.004454

56. Ghelfi P, Laghezza F, Scotti F, Serafino G, Capria A, Pinna S, et al. A fully photonics-based coherent radar system. *Nature.* (2014) **507**:341–5. doi: 10.1038/nature13078

57. Murmann B. *ADC Performance Survey 1997–2017 (ISSCC and VLSI Symposium).* Techical Report (2017).

58. Bouchand R, Xie X, Giunta M, Hänsel W, Lezius M, Holzwarth R, et al. Compact low-noise photonic microwave generation from commercial low-noise lasers. *IEEE Photon Technol Lett.* (2017) **29**:1403–6. doi: 10.1109/LPT.2017.2723821

59. Yang G, Zou W, Yu L, Chen J. Influence of the sampling clock pulse shape mismatch on channel-interleaved photonic analog-to-digital conversion. *Opt Lett.* (2018) **43**:3530. doi: 10.1364/OL.43.003530

60. Constans L, Combrié S, Sanchez D, Raineri F, de Rossi A. All-optical sampling of a 40 GHz signal using hybrid Silicon nanophotonics. In: OSA, editor. *Advanced Photonics 2018 (BGPP, IPR, NP, NOMA, Sensors, Networks, SPPCom, SOF).* Zurich: Optical Society of America (2018). p. IM3B.4.

61. Esman DJ, Wiberg AO, Yang MH, Liu L, Kuo BPP, Alic N, et al. Photonic parametric sampled analog-to-digital conversion at 100 GHz and 6 ENOBs. In: *2014 The European Conference on Optical Communication (ECOC).* Cannes: IEEE (2014). p. 1–3.

62. Gevorgyan H, Al Qubaisi K, Dahlem MS, Khilo A. Silicon photonic time-wavelength pulse interleaver for photonic analog-to-digital converters. *Opt Express.* (2016) **24**:13489–99. doi: 10.1364/OE.24.013489

63. Liu W, Li M, Guzzon RS, Norberg EJ, Parker JS, Lu M, et al. A fully reconfigurable photonic integrated signal processor. *Nat Photon.* (2016) **10**:190. doi: 10.1038/nphoton.2015.281

64. Wang J, Paesani S, Ding Y, Santagati R, Skrzypczyk P, Salavrakos A, et al. Multidimensional quantum entanglement with large-scale integrated optics. *Science.* (2018) **360**:285–91. doi: 10.1126/science.aar7053

65. Choudhary A, Morrison B, Aryanfar I, Shahnia S, Pagani M, Liu Y, et al. Advanced integrated microwave signal processing with giant on-chip Brillouin gain. *J Lightw Technol.* (2016) **35**:846–54. doi: 10.1109/JLT.2016.2613558

66. Marpaung D, Yao J, Capmany J. Integrated microwave photonics. *Nat Photon.* (2019) **13**:80. doi: 10.1038/s41566-018-0310-5

67. Ji H, Galili M, Hu H, Pu M, Oxenlowe LK, Yvind K, et al. 1.28-Tb/s demultiplexing of an OTDM DPSK data signal using a silicon waveguide. *IEEE Photon Technol Lett.* (2010) **22**:1762–4. doi: 10.1109/LPT.2010.2084566

68. Da Ros F, Yankov MP, da Silva EP, Pu M, Ottaviano L, Hu H, et al. Characterization and optimization of a high-efficiency AlGaAs-on-insulator-based wavelength converter for 64-and 256-QAM signals. *J Lightw Technol.* (2017) **35**:3750–7. doi: 10.1109/JLT.2017.2722013

69. Pu M, Hu H, Ottaviano L, Semenova E, Vukovic D, Oxenløwe LK, et al. Ultra-efficient and broadband nonlinear AlGaAs-on-insulator chip for low-power optical signal processing. *Laser Photon Rev.* (2018) **12**:1800111. doi: 10.1002/lpor.201800111

70. Yariv A, Koumans R. Time interleaved optical sampling for ultra-high speed A/D conversion. *Electron Lett.* (1998) **34**:2012–3.

71. Stepanovic D, Nikolic B. A 2.8 GS/s 44.6 mW time-interleaved ADC achieving 50.9 dB SNDR and 3 dB effective resolution bandwidth of 1.5 GHz in 65 nm CMOS. *IEEE J Solid State Circuits.* (2013) **48**:971–82. doi: 10.1109/JSSC.2013.2239005